International Journal of Heat and Mass Transfer 65 (2013) 339–347

Contents lists available at SciVerse ScienceDirect

International Journal of Heat and Mass Transfer

journal homepage: www.elsevier.com/locate/ijhmt

Particle image velocimetry measurement of jet impingement in a cylindrical chamber with a heated rotating disk

Yao-Hsien Liu [a,*], Li-Wei Tseng [a], Chih-Yung Huang [b], Kung-Liang Lin [b], Chien-Chih Chen [b]

[a] Department of Mechanical Engineering, National Chiao-Tung University, Hsinchu 30010, Taiwan
[b] Department of Mechanical and Systems Research Laboratories, Industrial Technology Research Institute, Hsinchu 31040, Taiwan

ARTICLE INFO

Article history:
Received 21 February 2013
Received in revised form 15 May 2013
Accepted 9 June 2013
Available online 4 July 2013

Keywords:
Flow field
Particle image velocimetry
Jet impingement
Rotating disk
Chemical vapor deposition

ABSTRACT

We studied the flow field of a jet impingement on a rotating heated disk to simulate the flow field surrounding the rotating disk of a chemical vapor deposition (CVD) reactor, which is widely used for large-scale production of thin-films and semiconductor materials. The flow field influences the growth rate and deposition uniformity, and is subject to the combined effects of buoyancy, centrifugal, and flow inertia forces that occur during the deposition process. The study investigated various flow-cell sizes and locations, such as the inlet flow-rate (1–10 slpm), jet-to-disk temperature difference (40–80 °C), and disk rotational speeds (0–500 rpm). Particle image velocimetry (PIV) was used to measure the flow-velocity field and flow-streamlines in the test chamber. The time-averaged axial and radial velocity profiles near the disk were used to determine the variations in flow velocity resulting from rotation and heating. Upward buoyancy forces, caused by the heated disk, produce flow cells and break the flow uniformity above the disk. When the rotational Reynolds number increases, the rotational effect eventually dominates the flow field that increases the flow velocity and generates flow cells near the chamber wall. Flow regime maps of these flow patterns were constructed, based on the Grashof number and rotational Reynolds number.

1. Introduction

Chemical vapor deposition (CVD) is a widely used process for the manufacture of high-brightness LEDs, thin-film solar cells, and other optoelectronic components. Large-scale CVD production can be achieved by the deposition in a vertical cylindrical reactor. The deposition rate and the film-thickness uniformity are highly sensitive to the reaction chamber geometry, reaction pressure, inlet-flow flange design, wafer carrier temperature, and the carrier-gas flow rate. Inside the reactor, abrupt changes in the flow velocity or flow recirculation above the substrate are detrimental to the uniformity of the deposition. These deleterious effects can be minimized or eliminated by optimizing the reactor configuration and process parameters.

To improve the quality of CVD products, the fluid-flow behavior in the CVD reactor has been the subject of both theoretical and experimental research for more than two decades. Evans et al. [1,2] used numerical methods to describe the mixed convection behaviors of a rotating disk, and thus, simulated the vertical CVD reactor. Their simulation accounted for the buoyancy forces and for the effects of disk rotation, and revealed that non-uniform deposition can be improved by increasing the uniformity of the inlet flow and by increasing the substrate rotational speed. Joh and Evans [3] investigated the effects of varying the distance between the rotating disk and the inlet flow. Their 1D simulation showed that the heat transfer from the rotating disk becomes significantly more sensitive to the flow parameter and disk Reynolds number as the distance decreases. Also, the flow recirculation cell becomes smaller as the distance between the inlet and disk decreases. Weyburne and Ahem [4] tested the design and operation conditions in a water-cooled, close-spaced reactor that was used for the growth of III–V materials. The closer spacing between the injector and the susceptor leads to high utilization of the reactant gases as well as reduces residence time of the reactants on the substrate. Moreover, the convection flow cells can be suppressed to prevent non-uniform film deposition. Compared to a standard rotating-disk reactor, considerably better deposition efficiencies were achieved by close spacing, and they maintained excellent uniformity. Soong et al. [5] predicted the flow field in a rotating-disk metal-organic CVD reactor using numerical methods. They demonstrated that the epitaxial flatness can be tuned either by controlling the vortex under a rotationally dominant regime or by incorporating an inlet flow-control.

Flow measurement techniques have been applied to obtain the flow-field data from the CVD reactors. Horton and Peterson [6] used a Rayleigh light scattering system to measure the transient gas temperature in a simulated rapid CVD reactor. The flow field

* Corresponding author. Tel.: +886 35712121x55136.
E-mail address: yhliu@mail.nctu.edu.tw (Y.-H. Liu).

0017-9310/$ - see front matter © 2013 Elsevier Ltd. All rights reserved.
http://dx.doi.org/10.1016/j.ijheatmasstransfer.2013.06.018

Nomenclature

D_j	diameter of the jet hole (m)
g	gravitational acceleration (m/s^2)
Gr	Grashof number (=$g\beta\Delta TH^3/\nu^2$)
H	distance between the jet hole and the disk (m)
N	number of sampling images
Q	inlet volume flow rate (slpm)
r, z	radial and axial coordinates
R	radius of the rotating disk (m)
Re	Reynolds number (=$\rho V_j D_j/\mu$)
Re_ω	rotational Reynolds number (=$\omega R^2/\nu$)
T_i	inlet fluid temperature (°C or K)
T_R	reference temperature (=$\frac{T_w+T_i}{2}$, °C or K)
T_w	disk temperature (°C or K)
ΔT	temperature difference between the disk and the inlet fluid (°C or K)
V_j	jet flow velocity (m/s)
V_r, V_z	radial and axial velocity components (m/s)
β	thermal expansion coefficient (=$1/T_R$)
ε	standard error of mean values
η	position error
μ	dynamic viscosity of fluid (N S/m^2)
ν	kinematic viscosity (m^2/s)
ρ	density of fluid (kg/m^3)
σ	standard deviation
ω	rotational speed (rad/s)

was dominated by the momentum before heating, but became unstable when the Gr/Re^2 ratio reached a value of 5. Mathews and Peterson [7] conducted flow-visualization and gas-temperature measurements to determine the regions of interest for momentum-dominated, buoyancy-dominated, and unstable flows. They later defined these regions as functions of the Grashof number, Reynolds number, pressure, and wafer temperature. Cheng et al. [8] studied the flow-field distribution in a CVD reactor using a flow-visualization smoke test, and investigated the convective vortex flow cells that were induced by the buoyancy and inertia forces by varying the pressure (300–760 Torr), jet-to-disk temperature differences (0–20 °C), and the inlet flow-rate (0.5–5 slpm). Their results revealed that lowering the chamber pressure reduces the buoyancy-driven circulation flows. They also pointed out that the variation of the air properties will be significant when the temperature difference between the jet and the heated disk is high. Setyawan et al. [9] investigated flow fields in a low-pressure (2.0–4.0 Torr) parallel plate CVD reactor because in high-temperature chambers, the particle trajectories are influenced by pressure. They showed that thermophoresis effects, resulting from the temperature gradient caused by heating the wafer-substrate plate, are pronounced for gas pressures of 2.0 and 4.0 Torr. Memon and Jaluria [10] experimentally investigated the flow structure and heat transfer in an impinging jet CVD reactor under atmospheric pressure. They investigated the momentum-driven and buoyancy-induced flow structures, and reported heat transfer correlations.

The reactor design has a significant impact on the flow-field distribution, and suppressing the buoyancy-induced flow recirculation can improve the epitaxial uniformity. Several techniques have been applied to reduce the flow recirculation, including inclining the reactor wall [11], tilting the cylinder head [12], and using rounded corners [13]. In addition, a uniform deposition is achievable by optimizing the processing parameters. Vanka et al. [14,15] numerically predicted the flow field in a CVD reactor; using an optimal inlet flow rate, substrate rotational rate, and reactor dimensionless length, the impinging jet reactor could be operated in atmospheric pressure without detrimental effects to the buoyancy-induced flow. Recently, Reinhold-López et al. [16] used particle image velocimerty to characterize the flow field in a vertically oriented cold wall reactor. The substrate surface temperature is up to 953 K and the gas flow rate ranged from 57 to 100 SCCM. Based on the results, the residence time curves and the minimum impingement time have been estimated.

Rotating-disk CVD reactors are popular for the production of large wafers because they offer better averages of the deposition distribution. The disk's rotation alters the buoyancy-induced and momentum-driven flows, which strongly influence the flow stability and uniformity of the deposition thickness. Biber et al. [17] showed that flow regime maps in a vertical rotating-disk reactor can be characterized as (1) plug-flow; the flow travels smoothly over the surface without causing any flow circulation in the reactor; (2) buoyancy-induced flow, in which an upward flow and recirculation forms during heating; and (3) rotationally induced flow, in which a toroidal vortex forms above the disk in the vicinity of the reactor wall. Plug-flow regimes are preferred for more uniform deposition. Kadinski et al. [18] numerically investigated the GaN/InGaN deposition in MOCVD vertical rotating-disk reactors. Their findings indicated that improvements in growth uniformity and alkyl efficiency are possible by modifying the alkyl injection system. Kim et al. [19] investigated the numbers of the injection holes and the rotating speed of the susceptor in a vertical RF-PECVD reactor. They concluded that the susceptor rotational speed has a significant effect, and that the buoyancy-induced flow should be prevented to provide greater efficiency and uniformity. Mitrovic et al. [20] investigated how flow stability is affected by a wide range of process parameters in the vertical rotating-disk MOCVD reactor, including the chamber pressure (10–1000 Torr), wafer rotational rate (0–1500 rpm), growth temperature (100–1100 °C), and the total gas flow rate (10–350 slpm). The flow regime can also be characterized by flow type as plug flow, buoyancy-induced flow, and rotation-induced flow. Flow recirculation due to the buoyancy force can be suppressed by increasing the total flow rate in the reactor or by decreasing the pressure. The literature contains reports of the optimization of the reactor design and process conditions [21,22]. Although numerical studies are readily available, detailed experimental reports of the effects of disk rotation on the flow field in a rotating-disk CVD reactor are scarce.

The objectives for this study were (1) to measure the flow velocity and flow streamlines using particle image velocimetry (PIV), which is more effective than traditional smoke visualization methods, because PIV provides spatial and temporal resolution; (2) the effects of the disk rotation and heating on the flow velocity above the substrate are investigated; and (3) a flow regime map is established to identify the plug flow, buoyancy-induced flow, and rotationally induced flow regimes in the test chamber.

2. Experimental setup and procedure

2.1. Particle image velocimetry system

Flow structures were investigated using PIV (TSI, MN, USA) (Fig. 1). The system comprises an Nd-YAG laser (λ = 532 nm) with a Q-switch module to control the pulsed laser energy to

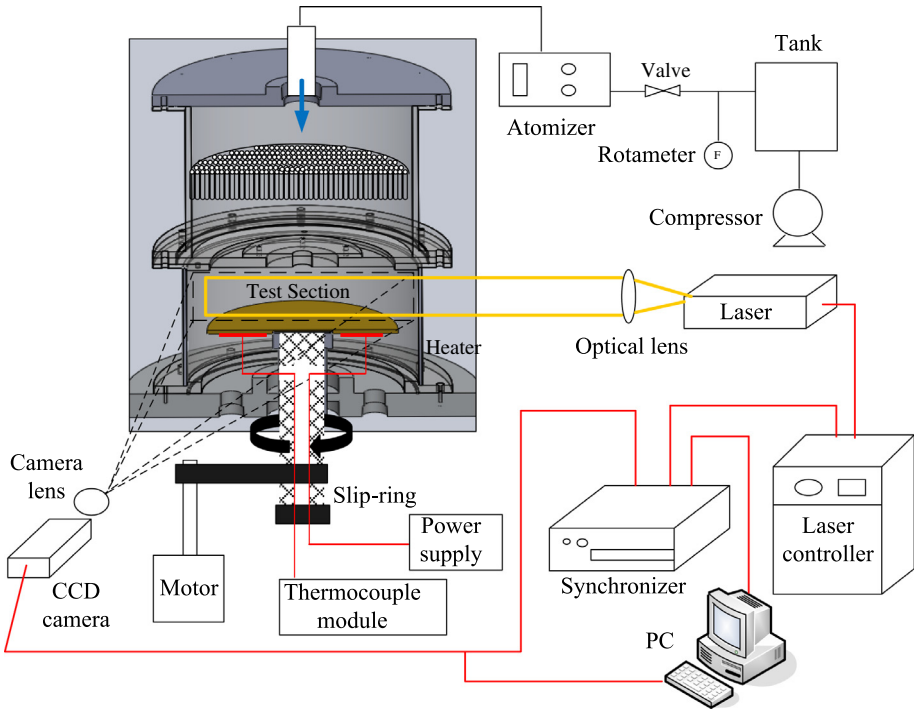

Fig. 1. Schematic diagram of the experimental setup.

100 mJ/Pulse. The pulse duration ranged from 0.6 to 6 ms, depending on the flow conditions. A laser light sheet was produced by passing the laser beam through a set of cylindrical and spherical lenses. A six-jet atomizer (Model 9306A, TSI) was used to produce seed particles from a sugar solution. Images of the seed particles in the flow field were captured by camera (PIVCAM 10–30, 1008 × 1018 pixels) and a frame grabber. The timing and control of the PIV system was provided by a synchronizer module (Model 610034) connected to the computer, CCD camera, and the pulsed laser. The commercial software (INSIGHT 3.3) that accompanied the PIV system was used to synchronize the laser and CCD camera, and was also used for data post-processing. The software used a standard cross-correlation scheme to process pairs of particle images with the Faster Fourier Transform (FFT). The flow-velocity vectors were calculated based on 32 × 32 pixel interrogation spots, which corresponded to approximately 6.7 mm square grids in the actual object plane of the test chamber.

2.2. Test chamber

We built a test chamber to model the flow field inside a rotating-disk CVD reactor (Fig. 2). The airflow is provided by a 1.5 hp air compressor, and a rotameter is used to measure the flow rate. The air flows into a mixing chamber, and mesh screens are placed

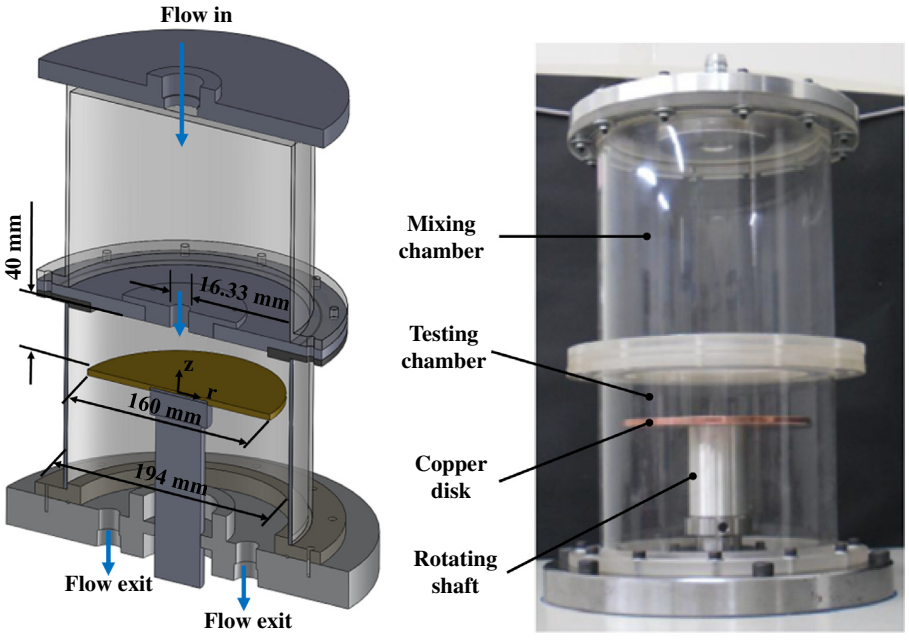

Fig. 2. The test chamber.

to improve flow distribution. The air then passes through a circular jet hole with a diameter of 16.33 mm and enters the testing chamber as the hole widens to a diameter of 194 mm. The flow impinges on a heated copper disk and exhausts through holes in the underside of the chamber. The acrylic cylindrical casing is 3 mm thick. A 160 mm diameter copper disk is connected to a rotating shaft that is driven by a frequency-controlled motor. Two blind holes are drilled beneath the copper disk for the installation of T-type thermocouples, and a silicone-rubber heater is attached to the bottom of the copper disk. A slip-ring (Mercotac H-6) was used to transmit power for the heater and signals from the thermocouples during operation. The disk rotates at speeds from 0 to 500 rpm. A thermocouple module (NI 9213) that is connected to a PC is used to monitor the temperature. During normal operation, the disk is heated until it reaches a steady state before the flow-field measurements are performed. The steady state is determined when there is less than ±0.3 °C variation in the substrate temperature, typically 2–2.5 h.

2.3. PIV error analysis due to optical distortion

As light passes through the inhomogeneous medium, the optical distortion results in a blurred image or causes particle image deformation [23]. Geometrical distortion of the particle image can cause position and velocity errors in the PIV measurements. The following model was developed to quantify the measurement error because of the light refracting through a curved surface, and is based on a method proposed by Murphy and Adrain [24]. Fig. 3 demonstrates the light refraction model as the laser light sheet passes through the center of the hollow cylinder. The calculated position error ratio (E) is defined as

$$E = \frac{(r_p - r_o) - \left(r'_p - r'_o\right)}{r'_p - r'_o} = \frac{\Delta r - \Delta r'}{\Delta r'} \times 100\%$$

where r'_p and r_p are the perceived and true positions of a particle, respectively. The r'_o and r_o variables are the reference origins of the specified particle's location in the refraction model. The particle moves from position r_o to position r_p during two successive pulses. The equation represents the difference between the perceived displacement $\Delta r'$ and the true displacement Δr of the particles in the measurement plane. A laser beam is diffracted twice when it passes from a medium with a lower refractive index (air, $n = 1.00227$) to a medium with a higher refractive index (acrylic, $n' = 1.46$), and then returns to the low refractive index medium (Fig. 3). The relationship between incident angle and refracted angle is provided by the Snell law:

$$n \times \sin\theta_1 = n' \times \sin\theta'_1 \quad \text{and} \quad n' \times \sin\theta_2 = n \times \sin\theta'_2$$

The governing equations for the light paths can be obtained from the optical geometry; consequently, the perceived particle position r'_p can be calculated. Fig. 4 shows a plot of the calculated position error ratio versus the location (r/R). Smaller particle displacements have greater position errors; the greatest position errors occur when the particles are close to the chamber wall. Data that were acquired from too near the wall ($r/R > 1.15$) were removed, thereby controlling the maximum position error to within 3.4%.

2.4. Uncertainty analysis

The uncertainty analysis of the test parameters was based on a method proposed by Kline and McClintock [25] (Table 1). The uncertainty analysis of the PIV measurement was based on a methodology by Son et al. [26]. With the time-averaged flow-velocity measurement from a number of N-sampling images, the uncertainty in the PIV measurement is assumed to be approximately equal to the standard error in the mean value:

$$\varepsilon = \sigma/\sqrt{N}$$

where, σ is the standard deviation of the measurement. With a sufficiently large number of sampling images, the central limit theorem states that these samples have an approximately normal distribution. The uncertainty in the velocity measurement is based on the standard error of the mean value and the average flow velocity. This calculation is based on 50 velocity measurement samples and the maximum uncertainty is within ±3%.

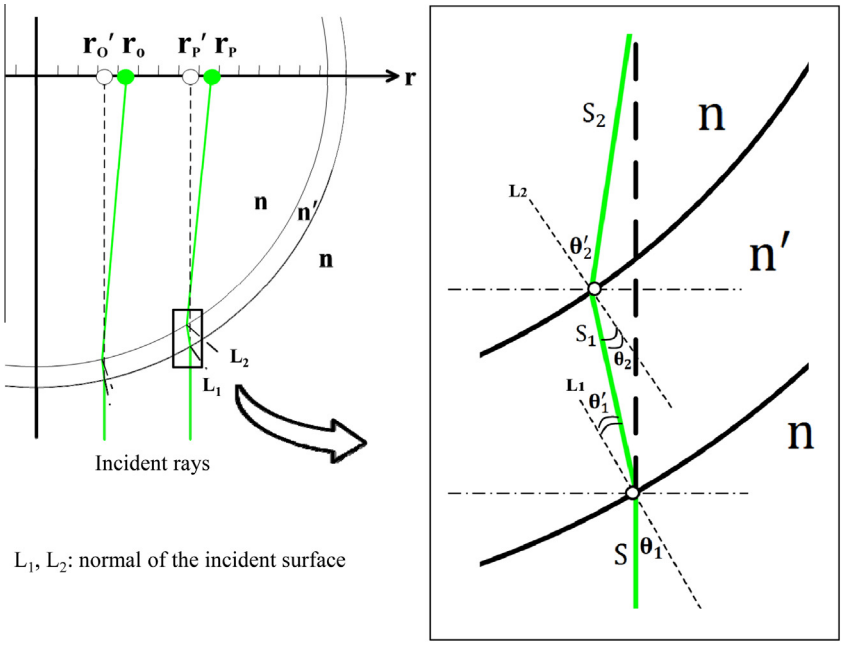

Fig. 3. Refraction model diagram. The green solid symbol and solid line represent the actual particle position and refracted light path, respectively.

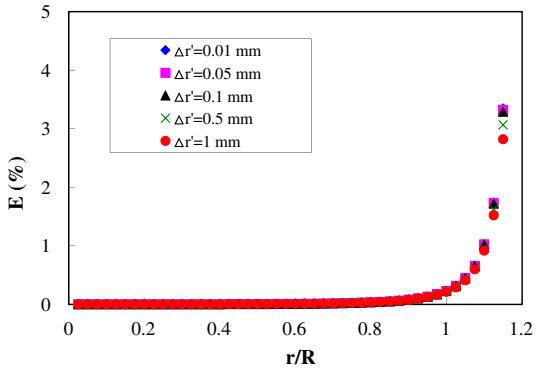

Fig. 4. Ratio of the position error (E).

Table 1
Uncertainties in test parameters.

Parameter	Uncertainty
D_j, R, H (m)	±0.1 mm
Q (L/min)	±3%
$\triangle T$ (°C or K)	±0.5 °C or K
μ (m/s^2)	±0.5%
ω (rpm)	±0.1 rpm
Re	±3.2%
Re_ω	±1%
Gr	±4%
ε (m/s)	±0.00134 m/s
V_r, V_z (m/s)	±3%

3. Results and discussion

We investigated the inlet flow-rate (Q) from 1 to 10 slpm; the temperature difference between the inlet flow and disk (ΔT) was varied from 0 to 80 °C, and the disk rotational speed (ω) was varied from 0 to 500 rpm. All experiments were performed at atmospheric pressure. The flow-field time-averaged flow was determined based on a steady or statistically stable state.

3.1. Flow distribution for a non-rotating disk

Observation of the flow patterns around a non-rotating disk can demonstrate the effects of the buoyancy force on the flow field. The effects of three inlet flow-rates (1, 2, and 5 slpm) and two jet-to-disk temperature differences (ΔT = 40 and 80 °C) on the flow-field distribution were investigated (Fig. 5). The Grashof number quantifies the ratio of the buoyancy force to the viscous force; it is provided by

$$Gr = \frac{g\beta\Delta T H^3}{\nu^2}$$

The properties are determined at the reference temperature (T_R). After the laminar jet impinged the substrate, the flow moved radially outward across the disk, until it was lifted by the buoyancy force. The vertically moving flow continued until it reached the upper surface, where it deflected and moved both radially inward and outward. This buoyancy-induced flow phenomenon produces a pair of inner flow cells and a pair of outer recirculation flow cells within the chamber.

The formation of these flow cells is dependent on the relative magnitudes of the inertia and buoyancy forces. The location from which the flow is lifted by the buoyancy force shifts from r/R = 0.4 to r/R = 0.9 when the inlet flow rate increases from 1 (Re = 63) to 2 slpm (Re = 125). The vertically moving flow induced by the buoyancy force shifts outward radially because of the increasing flow velocity across the disk. This results in larger inner flow cells and smaller outer recirculation flow cells. While the inlet flow rate increases to 5 slpm (Re = 314), the greater inertia force suppresses the vertical flow, and a single vortex flow cell replaces the two flow cells that were observed at lower flow rates, resulting in an inertia-driven flow pattern.

Effect of the buoyancy force can be investigated as the temperature difference increases from 40 (Gr = 181–912) to 80 °C (Gr = 342–423). When the inlet flow-rate increases, the buoyancy effect diminishes so that no significant difference between the flow fields is produced by these two heating conditions. Changing the inlet flow-rate has a greater effect on the flow field than altering the disk temperature for the cases shown in Fig. 5. The

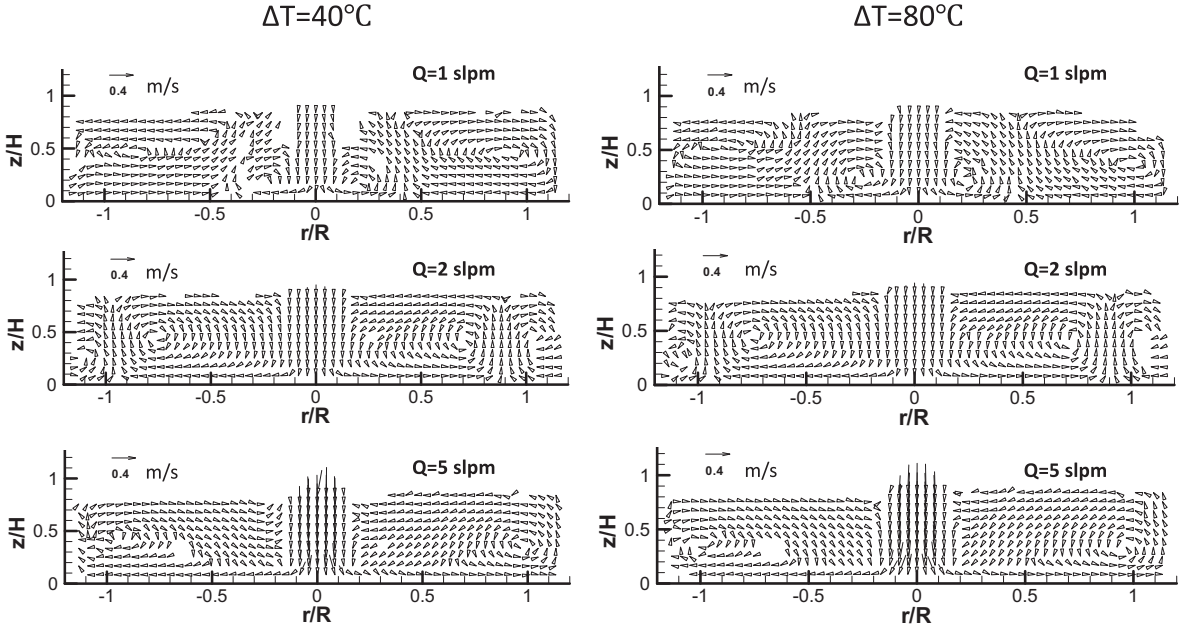

Fig. 5. Effect of inlet flow-rate and disk heating on the flow field for a non-rotating disk.

buoyancy-driven flow cells have detrimental effects on the flow-field uniformity and deposition rate, and thus, are undesirable for the CVD process. Another method, not examined in this study, is to reduce the chamber height, thereby substantially reducing the Grashof number and suppressing the flow-cell formation.

3.2. Flow distribution for a rotating disk

The effects of rotation on an unheated disk were first investigated free from the influence of the buoyancy-induced flows. The lowest inlet flow rate of 1 slpm was selected to demonstrate the effects of five rotational speeds (ω = 25, 50, 100, 250, and 500 rpm) (Fig. 6). The rotational Reynolds number was used to quantify the effects of the centrifugal force and the viscous force, where

$$Re_\omega = \frac{\omega R^2}{v}$$

Under disk rotation, the centrifugal forces pushed the flow radially outward across the disk surface, resulting in the attraction of the gas toward the disk surface. At the lowest rotational speed of 25 rpm (Re_ω = 807), the jet impinged the disk and flowed radially outward across the disk until it reached the chamber wall. A pair of rotationally induced flow cells formed near the chamber wall. Increasing the rotational speed increased the centrifugal force and caused the flow to accelerate. With the increase in the rotational Reynolds number, the flow cell-induced rotational velocities also increased. At 250 rpm (Re_ω = 8067), a pair of high-velocity flow cells formed close to position r/R = 1. At the greatest rotational speed of 500 rpm (Re_ω = 16134), these rotationally induced flow cells became more significant.

The combined effects of heating and rotation were studied; the effects of a rotating heated disk on the flow field for ΔT = 40 °C are shown in Fig. 7. The flow field with the stationary disk (0 rpm) is included for comparison. At 50 rpm (Re_ω = 1613), the centrifugal force suppressed the buoyancy flow-lifting effect. The vertical flow was radially forced outward, causing the buoyancy-induced flow cells to manifest near the chamber wall. The rotationally induced flow cells were relatively small at low rotational speeds; however, when the speed increased to 100 rpm (Re_ω = 3227), the buoyancy-induced flow became insignificant and the rotationally induced flow cell grew and expanded near the chamber wall. While the rotational speed continued to increase, the centrifugal force dominated the flow field and produced a pair of rotationally induced flow cells near the chamber wall.

The effects of the buoyancy force on the flow field were investigated by varying the temperature difference (ΔT = 40 and 80 °C) (Fig. 8). The rotational speed was fixed at 50 rpm, and the inlet flow-rate was fixed at 1 slpm. Unlike the unheated disk case, both of the heated cases featured buoyancy- and rotationally induced vortexes coexisting in the CVD chamber. With disk rotation, the vortex was pushed away from the disk by the centrifugal force, which prevented unstable flow cells from forming at the disk surface and helped improve the uniformity of the deposition. Because these rotationally induced flow cells were generally near the chamber wall, their influence on the flow field above the substrate was relatively small. In addition, the vertical buoyancy flow moved away from the center, reducing the risk of interruptions to the uniformity of the flow.

3.3. Velocity distribution

To understand the effects of rotation and heating on the flow-velocity distribution, and thus, determine when abrupt changes

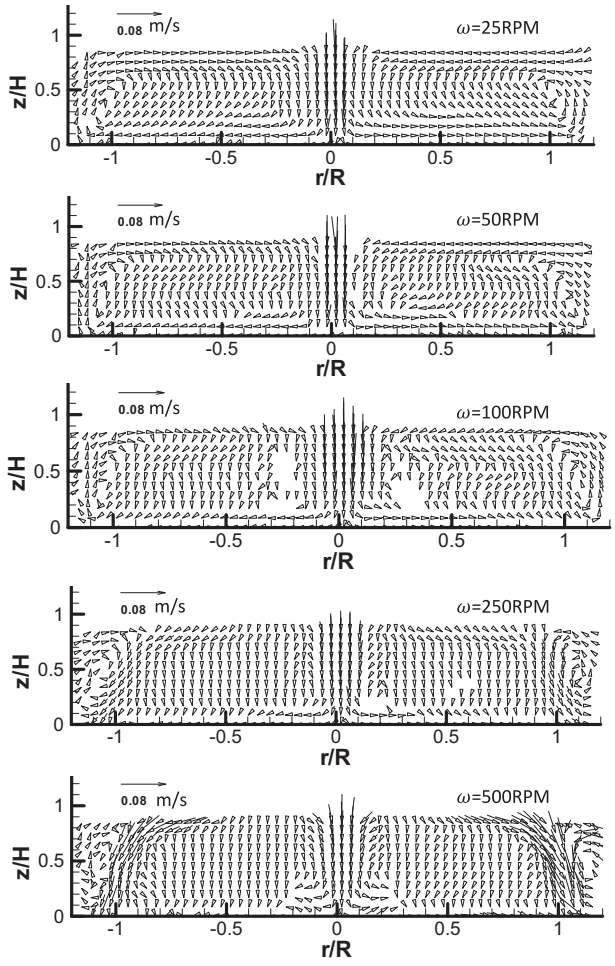

Fig. 6. Flow-field distribution for the unheated rotating disk (ΔT = 0 °C, Q = 1 slpm).

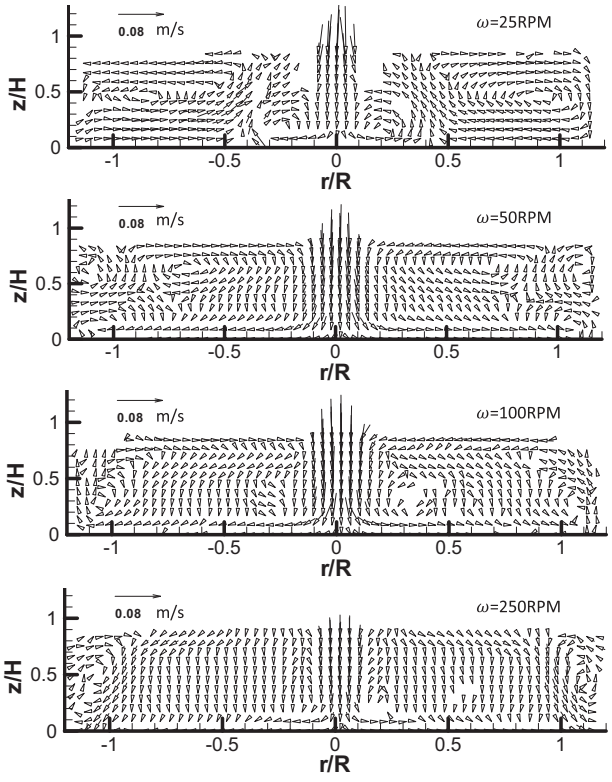

Fig. 7. Flow-field distribution for the heated rotating disk (ΔT = 40 °C, Q = 1 slpm).

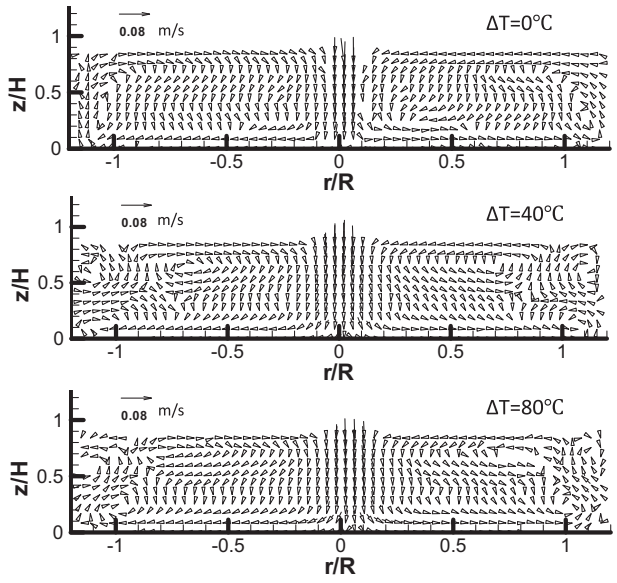

Fig. 8. Effect of temperature difference on the flow-field distribution (Q = 1 slpm, ω = 50 rpm).

in the flow velocity might occur, the time-averaged axial and radial velocity profiles that corresponded to the first row of the velocity vectors from PIV measurement for the flow field above the rotating disk were investigated (Fig. 9). The radial velocity (V_r) profile close to the disk oscillated between negative and positive values. A generally increasing trend in flow velocity was observed for both the heated (ΔT = 80 °C) and unheated (ΔT = 0 °C) cases when the rotational speed increased because of the increasing centrifugal force. Buoyancy-induced flow cells also caused radial flow acceleration near the center of the disk (r/R = 0). The buoyancy effect is significant for relatively small inertia forces (Q = 1 slpm). The axial flow velocity (V_z) has negative values, indicating that the flow moves inwards toward the center of the disk. In the rotating disk chamber, the greatest axial flow velocities occurred either in the center of the disk because of the impinging jet or close to the chamber wall because of the rotationally induced flow cells. For the heated disk, the centrifugal forces increased the velocity of the buoyancy-induced flow cells, producing greater axial velocities at the center of the disk than those observed for the unheated case. However, the axial flow above the disk, outside the disk center, and near the boundary was not strongly influenced by the rotation or heating, and the radial-flow velocity component was the dominant term. Spatial variations in the axial and radial flow velocities were more significant when the buoyancy force was present.

3.4. Analysis of flow regime

Figs. 10–13 show the flow-velocity fields and streamlines in a CVD chamber to illustrate the inertia-driven, buoyancy-induced, and rotationally induced flow patterns. Fig. 10 shows the inertia-driven flow pattern, which usually occurs in a chamber containing a stationary unheated disk. Without the effect of rotation and heating, the inlet flow impinged on the substrate and travelled radially outward across the disk. A pair of flow circulation cells is visible above the disk. Fig. 11 shows a heated disk, and demonstrates how the buoyancy force, caused by the temperature difference between the inlet gas and the disk, tends to lift the flow and drives the flow cells outwards. Compared to the flow field dominated by inertia, this buoyancy-induced flow produces a greater flow velocity in the inner vortex flow.

For a rotating disk, the centrifugal force pulls the flow radially outward, causing flow recirculation (Fig. 12). This occurred for both the heated and unheated disks because the rotational speed (ω = 100 rpm) for this demonstration was sufficient to suppress the buoyancy-induced flow behavior. However, under certain circumstances, the centrifugal force cannot suppress the

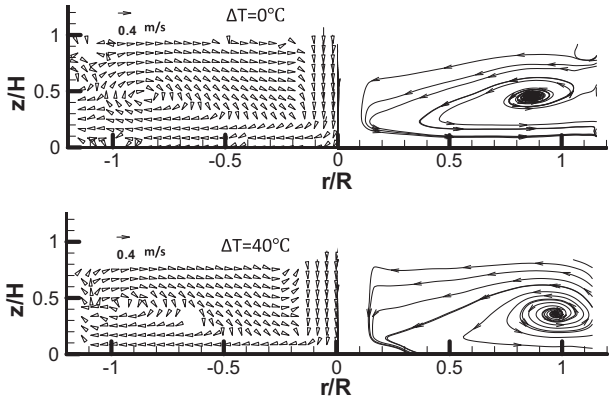

Fig. 10. Flow-velocity field and streamlines for the inertia-driven flow pattern (Q = 5 slpm, ω = 0 rpm).

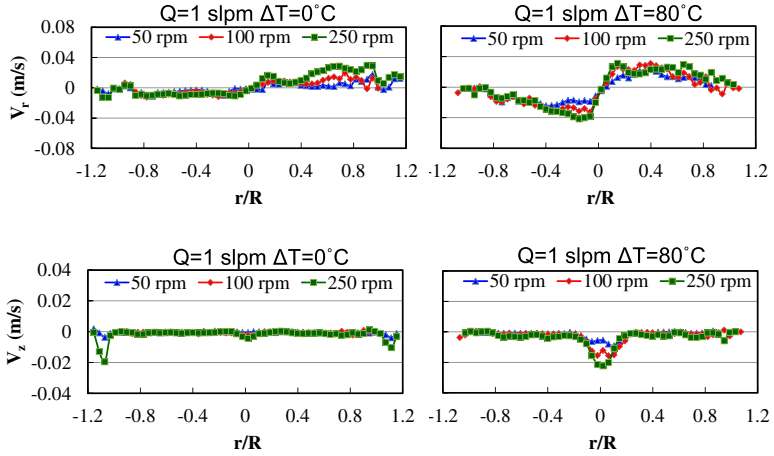

Fig. 9. Radial and axial velocity at the vicinity of the disk surface (z/H = 0.084).

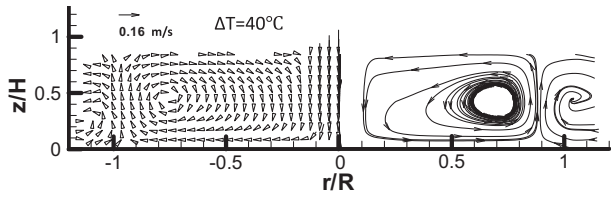

Fig. 11. Flow-velocity field and streamlines for the buoyancy-induced flow pattern (Q = 2 slplm, ω = 0 rpm).

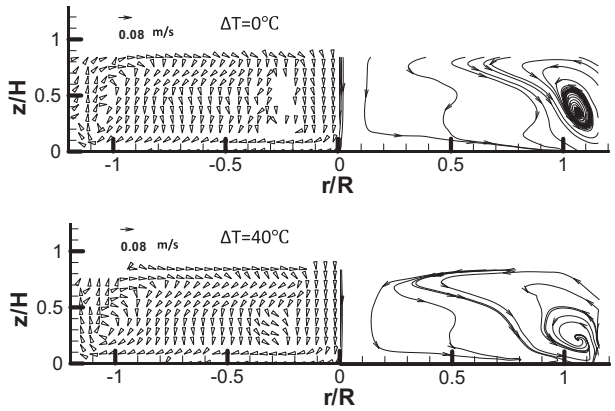

Fig. 12. Flow-velocity field and streamlines for the rotationally induced flow pattern (Q = 1 slplm, ω = 100 rpm).

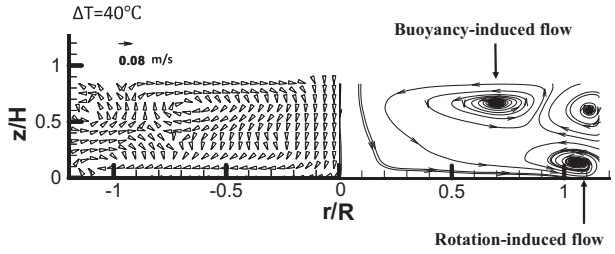

Fig. 13. Flow-velocity field and streamlines for the co-existing rotational and buoyancy-induced flow patterns (Q = 1 slplm, ω = 50 rpm).

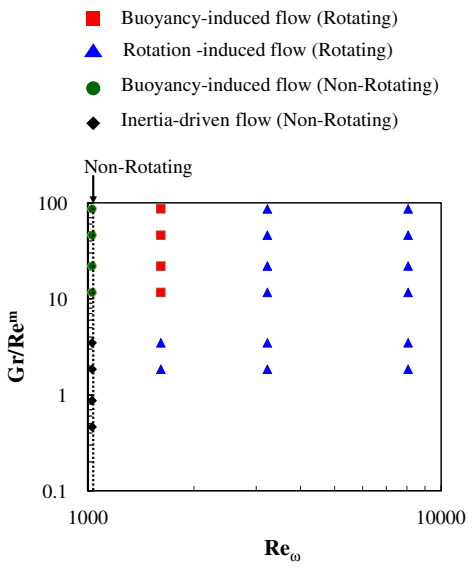

Fig. 14. Flow regime maps.

buoyancy-induced flow cells (e.g., at low rotational speeds and high disk temperatures). This competition between the buoyancy force and centrifugal force led to the coexistence of the rotationally induced and buoyancy-induced flow cells (Fig. 13).

Fig. 14 shows a flow regime map to correlate the three flow patterns based on the ratio of the buoyancy force to the inertia force (Gr/Re^m, $m = 2$) with respect to the rotational Reynolds number. The buoyancy-induced flow patterns typically occur for convection systems with high Grashof numbers or with small inertia forces, where the convection flow cells dominate the flow field at relatively low rotational Reynolds numbers. While the value of the rotational Reynolds number increases, the centrifugal force increasingly suppresses the buoyancy and inertia forces, thereby producing rotationally induced flow patterns. These dimensionless parameters are useful for quantifying the flow behaviors that occur for different processing parameters, such as the inlet flow rate, disk temperature, and rotational speed.

4. Conclusion

The flow patterns in a vertical cylindrical chamber with a heated rotating disk were investigated to simulate a CVD reactor, and the effects of the inlet flow-rate, jet-to-disk temperature differences, and disk rotational speeds on the flow field were determined. PIV was used to measure the magnitude and direction of the flow velocity. A flow regime map was established to predict the inertia-driven, rotationally induced, and buoyancy-induced flow patterns. The main conclusions are as follows:

(1) The three flow regimes are characterized by the dimensionless parameters: the Grashof number, the rotational Reynolds number, and the buoyancy force to inertia force ratio. The combined influence of the processing parameters on the flow field is predictable.
(2) The effects of the disk temperature are small compared to the specific CVD processes. Buoyancy-induced flow cells can dominate the flow field in the absence of significant inertial and centrifugal forces.
(3) Rotation causes greater flow velocities inside the chamber, suppresses the buoyancy-induced flow, and induces flow cells near the outer wall because these rotationally induced flow cells occurred close to the chamber wall. The influence of rotation on the variation in the spatial and temporal flow velocities above the substrate is relatively small compared to that of buoyancy-induced flows.
(4) When the temperature difference between the jet and disk is small, small variation occurs in the gas flow. High-temperature effects can be significant and may require further investigation before being successfully applied to a high temperature CVD process.

Acknowledgments

This study was funded by the Industrial Technology Research Institute and the National Science Council in Taiwan under contract No. NSC-100-2218-E-009-016.

References

[1] G. Evans, R. Greif, Effect of boundary conditions on the flow and hat transfer in a rotating disk chemical vapor deposition reactor, Numer. Heat Transfer 12 (2) (1987) 243–252.
[2] G. Evans, R. Greif, A numerical model of the flow and heat transfer in a rotating disk chemical vapor deposition reactor, J. Heat Transfer 109 (1987) 928–935.

[3] S. Joh, G.H. Evans, Heat transfer and flow stability in a rotating disk/stagnation flow chemical vapor deposition reactor, Numer. Heat Transfer Part A: Appl. 31 (8) (1997) 867–879.
[4] D.W. Weyburne, B.S. Ahem, Design and operating considerations for a water-cooled close-spaced reactant injector in a production scale MOCVD reactor, J. Cryst. Growth 170 (1997) 77–82.
[5] C.Y. Soong, C.H. Chyuan, R.Y. Tzong, Thermo-flow structure and epitaxial uniformity in large-scale metalorganic chemical vapor deposition reactors with rotating susceptor and inlet flow control, Jpn. J. Appl. Phys. 37 (10) (1998) 5823–5834.
[6] J.F. Horton, J.E. Peterson, Rayleigh light scattering measurements of transient gas temperature in a rapid chemical vapor deposition reactor, J. Heat Transfer 122 (2000) 165–170.
[7] A.G. Mathews, J.E. Peterson, Flow visualizations and transient temperature measurements in an axisymmetric impinging jet rapid thermal chemical vapor deposition reactor, J. Heat Transfer 124 (2002) 564–570.
[8] T.C. Cheng, P.H. Chiou, T.F. Lin, Visualization of mixed convective vortex rolls in an impinging jet flow of air through a cylindrical chamber, Int. J. Heat Mass Transfer 45 (16) (2002) 3357–3368.
[9] H. Setyawan, M. Shimada, K. Ohtsuka, K. Okuyama, Visualization and numerical of fine particle transport in a low-pressure parallel plate chemical vapor deposition reactor, Chem. Eng. Sci. 57 (3) (2002) 497–506.
[10] N. Memon, Y. Jaluria, Flow structure and heat transfer in stagnation flow CVD reactor, in: Proceedings of the 14th International Heat Transfer Conference, Washington, DC, 2010.
[11] C.Y. Shin, B.J. Baek, C.R. Lee, B. Pak, J.M. Yoon, K.S. Park, Numerical analysis for the growth of GaN layer in MOCVD reactor, J. Cryst. Growth 247 (2003) 301–312.
[12] J.C. Hsieh, C.W. Cheng, T.F. Lin, Suppression of buoyancy-driven vortex flow resulting from a low speed jet impinging onto a heated disk in a vertical cylinder by cylinder top tilting, Int. J. Heat Mass Transfer 47 (14–16) (2004) 3031–3045.
[13] G. Luo, S.P. Vanka, N. Glumac, Fluid flow and transport processes in a large area atmospheric pressure stagnation flow CVD reactor for deposition of thin films, Int. J. Heat Mass Transfer 47 (23) (2004) 4979–4994.
[14] S.P. Vanka, G. Luo, N.G. Glumac, Parametric effects on thin film growth and uniformity in an atmospheric pressure impinging jet CVD reactor, J. Cryst. Growth 267 (1–2) (2004) 22–34.
[15] S.P. Vanka, G. Luo, N.G. Glumac, Numerical study of mixed convection flow in an impinging jet CVD reactor for atmospheric pressure deposition of thin films, J. Heat Transfer 126 (5) (2004) 764–775.
[16] K. Reinhold-López, A. Braeuer, A. Schmitt, N. Popovska-Leipertz, A. Leipertz, Flow field characterization in a vertically oriented cold wall CCVD reactor by particle image velocimetry, Chem. Eng. J. 184 (2012) 315–325.
[17] C.R. Biber, C.A. Wang, S. Motakef, Flow regime map and deposition rate uniformity in vertical rotating-disk OMVPE reactors, J. Cryst. Growth 123 (1992) 545–554.
[18] L. Kadinski, V. Merai, A. Parekh, J. Ramer, E.A. Armour, R. Stall, A. Gurary, A. Galyukov, Yu. Makarov, Computational analysis of GaN/InGaN deposition in MOCVD vertical rotating disk reactors, J. Cryst. Growth 261 (2004) 175–181.
[19] Y.J. Kim, J.H. Boo, B. Hong, Youn J. Kim, Effects of showerhead shapes on the flowfields in a RF-PECVD reactor, Surf. Coat. Technol. 193 (2005) 88–93.
[20] B. Mitrovic, A. Gurary, L. Kadinski, On the flow stability in vertical rotating disk MOCVD reactors under a wide range of process parameter, J. Cryst. Growth 287 (2) (2006) 656–663.
[21] B. Mitrovic, A. Parekh, J. Ramer, Reactor design optimization based on 3D modeling of nitrides deposition in MOCVD vertical rotating disc reactor, J. Cryst. Growth 289 (2) (2006) 708–714.
[22] B. Mitrovic, A. Gurary, W. Quinn, Process conditions optimization for the maximum deposition rate and uniformity in vertical rotating disc MOCVD reactors based on CFD modeling, J. Cryst. Growth 303 (1) (2007) 323–329.
[23] G.E. Elsinga, B.W. van Oudheusden, F. Scarano, Evaluation of aero-optical distortion effects in PIV, Exp. Fluids 39 (2) (2005) 246–256.
[24] M.J. Murphy, R.J. Adrian, PIV through moving shock with refracting curvature, Exp. Fluids 50 (4) (2011) 847–862.
[25] S.J. Kline, F.A. McClintock, Describing uncertainty in single-sample experiments, Mech. Eng. 75 (1953) 3–8.
[26] S.Y. Son, K.D. Kihm, J.C. Han, PIV flow measurements for heat transfer characterization in two-pass square with smooth and ribbed walls, Int. J. Heat Mass Transfer 45 (24) (2002) 4809–4822.